



which gives rise, as discussed above, to valley-selective and spin-selective particle-hole excitations [4,19–23,29,35,36,41,42].

Aim of the present paper is to provide a compact and microscopical investigation of the onset of Kerr/Faraday rotation in a wide energy spectrum of single-layer TMDs. A key point is the identification of the orbital character of the particle-hole excitations at different energies allowed by the optical selection rules, and how it is reflected in the sign and strength of the optical Kerr/Faraday rotation. In order to address this issue in a clearest and controlled way, we introduce a proper generalization of a  $\mathbf{k} \cdot \mathbf{p}$  expansion in a three-band framework. The optical response is computed at the non-interacting level within a fully quantum Kubo approach where Kerr/Faraday effects are related to the appearing of off-diagonal components of the optical tensor. Different optical features are identified as associated with different particle-hole excitations, and their time evolution in out-of-equilibrium dynamics are discussed. While the exact energies of such optical features should be considered as unrenormalized by exciton binding effects (not considered here), the present work provides an analytical insight on the microscopic onset of the different optical features whose strengths can be conveniently modelled in terms of a unique parameter.

## 2. Single-particle Hamiltonian

Single-layer TMDs contain a plane of  $M$ -atoms in a triangular lattice, sandwiched between two layers of chalcogen atoms  $X$ . The resulting lattice, from a top view, appears as a bipartite hexagonal structure. Many theoretical approaches have been proposed to capture the relevant physics of these materials. As a general rule, effective low-energy models (like  $\mathbf{k} \cdot \mathbf{p}$  expansions) retain only the relevant conduction and valence bands, mapping the complex band structure onto an effective two-band gapped Dirac model [7,43–45]. On the other hand, tight-binding (TB) models have emphasized the role of the  $d$ -orbitals of the metal atoms, in particular the  $d_{3z^2-r^2}$ ,  $d_{xy}$ ,  $d_{x^2-y^2}$  ones, which provide the main orbital content of both the valence and conduction bands, as well as of a third higher-energy conduction band [46–53]. From a microscopical point of view, however, the simple triangular lattice of the  $M$  atoms cannot account for a gapped semiconducting band-structure, and the hybridization with  $X$  atoms has been shown to play a crucial role. The choice between a simplified, semi-analytical approach and the multiband complexity of a fully microscopical TB model is a delicate issue which depends on the physics on which to be focused.

An interesting balance between these two approaches has been provided by Liu *et al.* in Ref. [54] where they introduced a compact three-band tight-binding model within the reduced Hilbert space:

$$\phi_{\mathbf{p}}^{\dagger} = (d_{\mathbf{p},3z^2-r^2}^{\dagger}, d_{\mathbf{p},xy}^{\dagger}, d_{\mathbf{p},x^2-y^2}^{\dagger}), \quad (1)$$

where the role of the hybridization of the  $d$ -orbitals of  $M$  atoms with  $p$ -orbitals of  $X$  is modelled, using symmetry arguments, by means of effective complex hopping parameters that break the triangular symmetry, enforcing the physics of a bipartite hexagonal lattice. The resulting one-particle Hamiltonian can be thus written in the full Brillouin zone thus as:

$$\hat{H}_{\sigma}(\mathbf{k}) = \hat{H}_{\text{TB}}(\mathbf{k}) + \hat{H}_{\text{SO},\sigma}, \quad (2)$$

where interatomic hoppings up to third-nearest-neighbor level are included in the TB part  $\hat{H}_{\text{TB},\mathbf{k}}$ , providing an excellent agreement with ab-initio calculations for the conduction and valence bands close to the  $K$ ,  $K'$  valleys. The spin-orbit coupling (SOC) is safely approximated with its dominant contribution due to the local spin-diagonal term [54,55], which in this basis reads:

$$\hat{H}_{\text{SO},\sigma} = \lambda I_{\sigma} \begin{pmatrix} 0 & 0 & 0 \\ 0 & 0 & i \\ 0 & -i & 0 \end{pmatrix}, \quad (3)$$

where  $I_\sigma = \delta_{\sigma,\uparrow} - \delta_{\sigma,\downarrow}$ .

Such three-band tight-binding model provides an accurate description of the energy dispersion and of the orbital character of the main relevant bands for optical probes with the advantage of a reduced Hilbert space. In the following we focus on the optical response that is governed by the particle-hole excitations close to the K, K' valley points. The above model represents thus also a suitable platform for an analytical  $\mathbf{k} \cdot \mathbf{p}$  expansion that generalizes the previous  $\mathbf{k} \cdot \mathbf{p}$  approaches [7,43–45] up to the relevant three-orbital space. To this aim we thus expand  $\hat{H}(\mathbf{k})$  up to the quadratic order in the relative momentum  $\mathbf{p} = \mathbf{k} - \mathbf{K}$  ( $\mathbf{p} = \mathbf{k} - \mathbf{K}'$ ) close to the K, K'. It is also convenient to express the resulting Hamiltonian  $\hat{H}(\mathbf{p}, \mathbf{K})$ ,  $\hat{H}(\mathbf{p}, \mathbf{K}')$  in the chiral basis:

$$\psi_{\mathbf{p}}^\dagger = (d_{\mathbf{p},3z^2-r^2}^\dagger, d_{\mathbf{p},L}^\dagger, d_{\mathbf{p},R'}^\dagger), \quad (4)$$

where  $d_{\mathbf{p},L} = (d_{\mathbf{p},x^2-y^2} - id_{\mathbf{p},xy})/\sqrt{2}$  and  $d_{\mathbf{p},R} = (d_{\mathbf{p},x^2-y^2} + id_{\mathbf{p},xy})/\sqrt{2}$ . In such basis the spin-orbit term appears purely diagonal,

$$\hat{H}_{\text{SO},\sigma} = -\lambda I_\sigma \begin{pmatrix} 0 & 0 & 0 \\ 0 & 1 & 0 \\ 0 & 0 & -1 \end{pmatrix}, \quad (5)$$

and we can write:

$$\hat{H}(\mathbf{p}, \mathbf{K}) = \begin{pmatrix} E_0 + a_0 p^2 a^2 & v_{0/\text{T}}(p+a) & v_{0/\text{B}}(p-a) \\ v_{0/\text{T}}(p+a)^* & E_{\text{T}} + a_{\text{T}} p^2 a^2 & v_{\text{T}/\text{B}}(p+a) \\ v_{0/\text{B}}(p-a)^* & v_{\text{T}/\text{B}}(p+a)^* & E_{\text{B}} + a_{\text{B}} p^2 a^2 \end{pmatrix}, \quad (6)$$

$$\hat{H}(\mathbf{p}, \mathbf{K}') = \begin{pmatrix} E_0 + a_0 p^2 a^2 & -v_{0/\text{B}}(p+a) & -v_{0/\text{T}}(p-a) \\ -v_{0/\text{B}}(p+a)^* & E_{\text{B}} + a_{\text{B}} p^2 a^2 & -v_{\text{T}/\text{B}}(p+a) \\ -v_{0/\text{T}}(p-a)^* & -v_{\text{T}/\text{B}}(p+a)^* & E_{\text{T}} + a_{\text{T}} p^2 a^2 \end{pmatrix}, \quad (7)$$

where  $p_\pm = p_x \pm ip_y$ ,  $a$  is the in-plane M-M distance. The full expression of the band parameters in Eqs. (6)-(7) in terms of the original tight-binding parameters is provided in Appendix A. The total spin-full Hamiltonians at the K and K'

$$\hat{H}_\sigma(\mathbf{p}, \nu) = \hat{H}(\mathbf{p}, \nu) + \hat{H}_{\text{SO},\sigma}, \quad (8)$$

(where  $\nu = \text{K}, \text{K}'$ ) contain all the relevant entanglements between spin, valleys and chirality.

Eq. (8) defines the energy levels at the K point for each spin family. We have explicitly:

$$\epsilon_{\text{T},\sigma}(0) = E_{\text{T}} - \lambda I_\sigma, \quad (9)$$

$$\epsilon_{0,\sigma}(0) = E_0, \quad (10)$$

$$\epsilon_{\text{B},\sigma}(0) = E_{\text{B}} + \lambda I_\sigma. \quad (11)$$

At the K point, the energy level  $E_0$  corresponds to the conduction band edge, which results here spin-degenerate since we neglect the weak spin-orbit coupling of the X chalcogen atoms. The valence band at K is associated with the R-chiral state with spin-split energies  $E_{\text{B}} \pm \lambda$ , for up and down spin, respectively. The  $E_{\text{T}} \pm \lambda$  levels correspond to higher energy states, characterized by a L-chiral symmetry [47]. A similar energy spectrum is found at the K' point, but with chiral content exchanged between the valence and the high-energy levels.

The optical selection rules are encoded in the multiband matrix structure of the current operators which can be straightforwardly computed as derivatives of the single-particle

Hamiltonian,  $\hat{j}_i(\mathbf{p}, \nu) = dH(\mathbf{p}, \nu)/dp_i$ , where  $i = x, y$  and  $\nu = K, K'$ . At the high-symmetry points ( $\mathbf{p} = 0$ ) we get:

$$\hat{j}_x(K) = \begin{pmatrix} 0 & v_{0/T}a & v_{0/B}a \\ v_{0/T}a & 0 & v_{T/B}a \\ v_{0/B}a & v_{T/B}a & 0 \end{pmatrix}, \quad (12)$$

$$\hat{j}_y(K) = \begin{pmatrix} 0 & iv_{0/T}a & -iv_{0/B}a \\ -iv_{0/T}a & 0 & iv_{T/B}a \\ iv_{0/B}a & -iv_{T/B}a & 0 \end{pmatrix}, \quad (13)$$

$$\hat{j}_x(K') = -\begin{pmatrix} 0 & v_{0/B}a & v_{0/T}a \\ v_{0/B}a & 0 & v_{T/B}a \\ v_{0/T}a & v_{T/B}a & 0 \end{pmatrix}, \quad (14)$$

$$\hat{j}_y(K') = \begin{pmatrix} 0 & -iv_{0/B}a & iv_{0/T}a \\ iv_{0/B}a & 0 & -iv_{T/B}a \\ -iv_{0/T}a & iv_{T/B}a & 0 \end{pmatrix}. \quad (15)$$

In similar way, one can derive the chiral current operators  $\hat{j}_{\pm}(\nu) = \hat{j}_x(\nu) \pm i\hat{j}_y(\nu)$ :

$$\hat{j}_+(K) = \begin{pmatrix} 0 & 0 & 2v_{0/B}a \\ 2v_{0/T}a & 0 & 0 \\ 0 & 2v_{T/B} & 0 \end{pmatrix}, \quad (16)$$

$$\hat{j}_-(K) = \begin{pmatrix} 0 & 2v_{0/T}a & 0 \\ 0 & 0 & 2v_{T/B} \\ v_{0/B}a & 0 & 0 \end{pmatrix}, \quad (17)$$

$$\hat{j}_+(K') = \begin{pmatrix} 0 & 0 & -2v_{0/T}a \\ -v_{0/B}a & 0 & 0 \\ 0 & -v_{T/B}a & 0 \end{pmatrix}, \quad (18)$$

$$\hat{j}_-(K') = \begin{pmatrix} 0 & -2v_{0/B}a & 0 \\ 0a & 0 & -2v_{T/B}a \\ -2v_{0/T}a & 0a & 0 \end{pmatrix}. \quad (19)$$

In order to evaluate the optical response, Eq. (8) can be numerically diagonalized for finite momentum  $\mathbf{p}$  to obtain eigenvalues (the band dispersion) and eigenvectors of the resulting eigenstates. This task can be however further simplified within a  $\mathbf{k} \cdot \mathbf{p}$  framework where the band dispersion, at the quadratic order we are interested in, is simply provided by the diagonal terms of Eqs. (6)-(7) corrected by the second-order corrections resulting from the off-diagonal elements. We get thus:

$$\hat{H}_{\sigma}(\mathbf{p}, \nu) \approx \hat{E}_{\sigma}(\mathbf{p}, \nu), \quad (20)$$

where

$$\hat{E}_{\sigma}(\mathbf{p}, K) = \begin{pmatrix} \epsilon_{0,\sigma}(p) & 0 & 0 \\ 0 & \epsilon_{T,\sigma}(p) & 0 \\ 0 & 0 & \epsilon_{B,\sigma}(p) \end{pmatrix}, \quad (21)$$

$$\hat{E}_{\sigma}(\mathbf{p}, K') = \begin{pmatrix} \epsilon_{0,-\sigma}(p) & 0 & 0 \\ 0 & \epsilon_{B,-\sigma} & 0 \\ 0 & 0 & \epsilon_{T,-\sigma}(p) \end{pmatrix}, \quad (22)$$

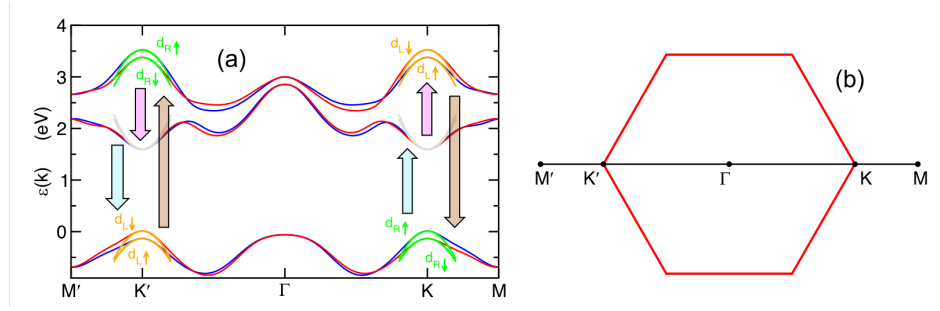


**Figure 1.** (a) Comparison between the three-band TB model from Ref. [54] and our analytical three-band  $\mathbf{k} \cdot \mathbf{p}$  model for single-layer MoS<sub>2</sub> along the path described in panel (b). Blue and red solid lines represent the TB band-dispersion for spin-up and spin-down electrons, respectively. Green, orange, and grey lines show the band-dispersions for the eigenstates with orbital character  $d_R$ ,  $d_L$ , and  $d_{3z^2-r^2}$ , respectively. The vertical arrows represent the optical interband transitions allowed at the K, K' points by a left-circularly polarized photon.

and where

$$\epsilon_{T,\sigma}(p) = E_T - \lambda I_\sigma + \bar{a}_{T,\sigma} p^2 a^2, \quad (23)$$

$$\epsilon_{0,\sigma}(p) = E_0 + \bar{a}_{0,\sigma} p^2 a^2, \quad (24)$$

$$\epsilon_{B,\sigma}(p) = E_B + \lambda I_\sigma + \bar{a}_{B,\sigma} p^2 a^2. \quad (25)$$

The numerical expression of the  $\mathbf{k} \cdot \mathbf{p}$  band parameters in Eqs. (23)-(25) is also provided in Appendix A. The comparison between the full TB dispersion in the Brillouin zone, from Ref. [54], and our analytical three-band model expanded around the K, K' points is displayed in Fig. 1, showing an excellent agreement.

Note that, within the same  $\mathbf{k} \cdot \mathbf{p}$  expansion, the leading order to the current operators is not affected and Eqs. (16)-(19) are still valid also in the  $\mathbf{k} \cdot \mathbf{p}$  context. As mentioned, the different matrix structure of Eqs. (16)-(19) enforces the different optical selection rules at the K and K' points. It is useful to recall that right-circularly polarized light (RCP) couples with the L-chiral current  $J_-$ , whereas LCP couples with  $J_+$ , according with the relation:  $A_x J_x + A_y J_y = [A_+ J_- + A_- J_+]/2$ . Eqs. (16)-(19) dictate for instance how, under external pumping conditions, absorption of a left-circularly polarized (LCP) photon can induce particle-hole optical excitations at the K point only between the valence band with  $d_R$  character and the conduction band with  $d_{3z^2-r^2}$  character, or (in case of electron-doped samples) between the conduction band with  $d_{3z^2-r^2}$  character and the high-level conduction band with  $d_L$  character. On the other hand, the same absorption of a LCP photon can effectively create particle-hole optical excitations at the K' point between the valence band with  $d_R$  character and the high-level conduction band with  $d_L$  character. The selection rules for right-circularly polarized light, coupled with the chiral current  $J_+$ , are graphically obtained by reversing the arrow of each particle-hole excitations.

Similar selection rules govern also the virtual processes involved in the optical linear response, whose analytical computation will be addressed in the next section.

### 3. Optical response

Equipped with the theoretical tools outlines in Section 2, we can now compute in the useful chiral basis all the elements of the optical tensor of single-layer transition-metal dichalcogenides through the evaluation of the frequency-dependent current-current response function. In the Matsubara space we have:

$$\pi_{ij}(i\hbar\omega_m, \nu) = \frac{e^2 T}{4\pi^2 \hbar^2} \sum_{\sigma, n} \int d^2 \mathbf{p} \text{Tr} \left[ \hat{f}_i(\nu) \hat{G}_\sigma(\mathbf{p}, i\omega_n + i\omega_m, \nu) \hat{f}_j^\dagger(K) \hat{G}_\sigma(\mathbf{p}, i\omega_n, \nu) \right], \quad (26)$$

where  $i, j = x, y, v = K, K'$ ,

$$\hat{G}_\sigma(\mathbf{p}, z, \nu) = \frac{1}{(z + \mu)\hat{I} - \hat{E}_\sigma(\mathbf{p}, \nu)}, \quad (27)$$

and where  $\mu$  is the chemical potential. Here  $\hbar\omega_n = \pi T(2n + 1)$  are the internal fermionic frequencies,  $\hbar\omega_m = 2\pi Tm$  is the external bosonic frequency, and  $T$  is the temperature.

The generic elements of the optical conductivity tensor are thus obtained as:

$$\sigma_{ij}(\omega, \nu) = -\frac{\pi_{ij}(\hbar\omega, \nu)}{i\omega}, \quad (28)$$

where

$$\pi_{ij}(\hbar\omega, \nu) = \pi_{ij}(i\hbar\omega_m, \nu)|_{i\omega_m \rightarrow \omega}. \quad (29)$$

Given the three-band structure of our model, the total optical response can be divided (leaving aside the Drude-like intraband terms at low frequencies which are not relevant in the present analysis) in three interband contributions:

$$\sigma_{ij}(\omega, \nu) = \sigma_{ij}^{0,T}(\omega, \nu) + \sigma_{ij}^{0,B}(\omega, \nu) + \sigma_{ij}^{T,B}(\omega, \nu). \quad (30)$$

The term  $\sigma_{ij}^{0,B}$  describes optical transitions between the (spin-split) valence band and the lowest energy conduction bands. Due to the spin-splitting of the valence band, this term accounts for the A and B exciton resonances. The term  $\sigma_{ij}^{T,B}$  conveys information about optical transitions between the valence band (with  $d_R$  or  $d_L$  character) and the high-energy conduction band with opposite  $d_R/d_L$  character, which has been discussed in details in Refs. [26,27]. Finally, the term  $\sigma_{ij}^{0,T}$  describes optical transitions between the lowest-energy and high-energy conduction bands. In the undoped semiconducting regime, due to the Pauli blocking, this term is usually irrelevant, but it plays a role upon photo-induced doping [26,27].

All the terms present a similar functional structure where the relevant role is played by the band population. For sake of simplicity, we focus thus for the moment on the first term  $\sigma_{ij}^{0,B}$ . Since the system is block-diagonal in the spin-index, one can also formally compute separately the optical response  $\sigma_{ij,\sigma}(\omega, \nu)$  for each spin and each valley  $\nu$ . We have for instance:

$$\begin{aligned} \sigma_{xx,\sigma}^{0,B}(\omega, \mathbf{K}) \approx & -\frac{e^2}{4\pi^2\hbar^2} \frac{(v_{0/B}a)^2}{\omega} \int d^2\mathbf{p} \left[ \frac{f[\epsilon_{0,\sigma}(p)] - f[\epsilon_{B,\sigma}(p)]}{\epsilon_{0,\sigma}(p) - \epsilon_{B,\sigma}(p) - \omega - i\delta} \right. \\ & \left. + \frac{f[\epsilon_{0,\sigma}(p)] - f[\epsilon_{B,\sigma}(p)]}{\epsilon_{0,\sigma}(p) - \epsilon_{B,\sigma}(p) + \omega + i\delta} \right], \end{aligned} \quad (31)$$

where  $f[E]$  is the occupation factor for given momentum and band, which under equilibrium conditions,  $f[E] = 1/\{\exp[(E - \mu)/T] + 1\}$ . At  $T = 0$ , in the semiconducting state  $\mu = 0$ , one get  $f[\epsilon_{0,\sigma}(p)] = 0$ ,  $f[\epsilon_{B,\sigma}(p)] = 1$  and, for  $\omega > 0$ :

$$\text{Re}\sigma_{xx,\uparrow}^{0,B}(\omega, \mathbf{K}) = \sigma_0 \frac{v_{0/B}^2}{c_A \hbar\omega} \theta(\hbar\omega - \Delta_A), \quad (32)$$

$$\text{Re}\sigma_{xx,\downarrow}^{0,B}(\omega, \mathbf{K}) = \sigma_0 \frac{v_{0/B}^2}{c_B \hbar\omega} \theta(\hbar\omega - \Delta_B), \quad (33)$$

where  $\sigma_0 = e^2/4\hbar$  is the universal two-dimensional conductivity,  $\Delta_A$ ,  $\Delta_B$  and the excitation edges for the A and B excitons, respectively,

$$\Delta_A = E_0 - E_B - \lambda, \quad (34)$$

$$\Delta_B = E_0 - E_B + \lambda, \quad (35)$$

and

$$c_A = \bar{a}_{0,\uparrow} - \bar{a}_{B,\uparrow}, \quad (36)$$

$$c_B = \bar{a}_{0,\downarrow} - \bar{a}_{B,\downarrow}. \quad (37)$$

Using the tight-binding parameters of Ref. [54], we get for MoS<sub>2</sub>  $\Delta_A = 1.584$  eV,  $\Delta_B = 1.730$  eV,  $v_{0/B} =$ ,  $c_A = 1.598$  eV, and  $c_B = 1.616$  eV. For symmetry we have also  $\sigma_{xx,\sigma}(\omega, \nu) = \sigma_{yy,\sigma}(\omega, \nu)$ .

In similar way, one gets:

$$\begin{aligned} \sigma_{xy,\sigma}^{0,B}(\omega, K) = & i \frac{e^2}{4\pi^2\hbar^2} \frac{(v_{0/B}a)^2}{\omega} \sum_{\mathbf{p}} \left[ \frac{f[\epsilon_{0,\sigma}(p)] - f[\epsilon_{B,\sigma}(p)]}{\epsilon_{0,\sigma}(p) - \epsilon_{B,\sigma}(p) - \omega - i\delta} \right. \\ & \left. - \frac{f[\epsilon_{0,\sigma}(p)] - f[\epsilon_{B,\sigma}(p)]}{\epsilon_{0,\sigma}(p) - \epsilon_{B,\sigma}(p) + \omega + i\delta} \right], \end{aligned} \quad (38)$$

and, for  $T, \mu = 0$  and  $\omega > 0$ :

$$\text{Im}\sigma_{xy,\uparrow}^{0,B}(\omega, K) = -\sigma_0 \frac{v_{0/B}^2}{c_A \hbar \omega} \theta(\hbar\omega - \Delta_A), \quad (39)$$

$$\text{Im}\sigma_{xy,\downarrow}^{0,B}(\omega, K) = -\sigma_0 \frac{v_{0/B}^2}{c_B \hbar \omega} \theta(\hbar\omega - \Delta_B). \quad (40)$$

The real parts of  $\sigma_{xy,\sigma}(\omega, K)$  and the imaginary parts of  $\sigma_{xx,\sigma}(\omega, K)$  can be thus easily obtained using the Kramers-Kronig relations. Furthermore, using the symmetry relations encoded in the different matrix structures at different valleys, one can recognize that at equilibrium:

$$\sigma_{xx,\sigma}^{0,B}(\omega, K') = \sigma_{xx,-\sigma}^{0,B}(\omega, K), \quad (41)$$

$$\sigma_{xy,\sigma}^{0,B}(\omega, K') = -\sigma_{xy,-\sigma}^{0,B}(\omega, K), \quad (42)$$

( $-\sigma$  being here the reversed  $\sigma$  spin), so that, under such equilibrium conditions, the contributions of different valleys *sum up* for the diagonal terms of the optical tensor, whereas they *cancel out* for the off-diagonal ones, in accordance with the time-reversal symmetry. The net result for the whole optical tensor is summarized in Fig. 2a. Similar expressions can be derived for the  $\sigma_{xy,\sigma}^{0,T}(\omega, \nu)$  and  $\sigma_{xy,\sigma}^{T,B}(\omega, \nu)$  terms.

#### 4. Non-equilibrium optical response

Eqs. (31), (38) provide a suitable framework to model the optical response under non-equilibrium conditions, by specifying the proper occupation factors in the presence of photo-induced particle-hole excitations. More specifically, within such semi-classical approach, we can simulate the effects of a LCP laser pumping tuned at the  $\omega \approx \Delta_A$  frequency by assuming an effective photoinduced charge transfer  $n_{\text{pump}}$  from the valence to the conduction band. Due to the selected circular polarization, such particle-hole excitations occur only at the K point and, due to the selected frequency in resonance with the A exciton, only for the

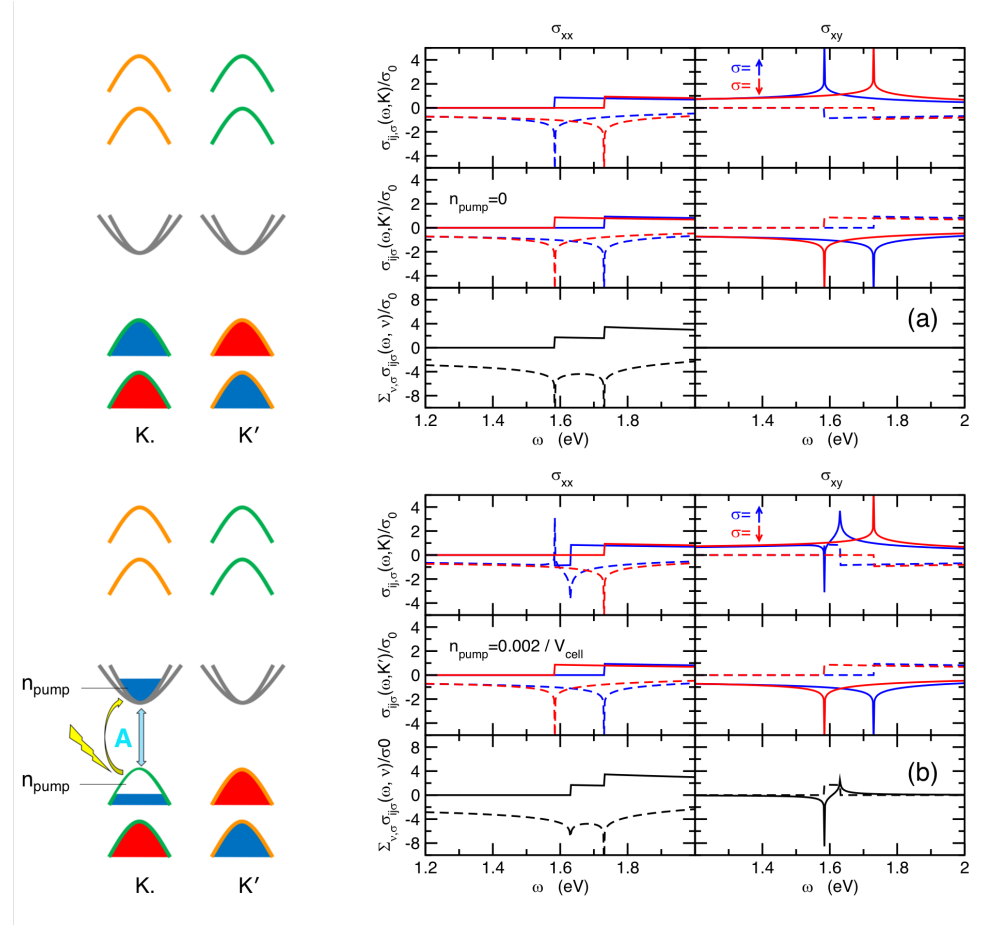


**Figure 2.** Plot of the different contributions to the diagonal  $\sigma_{xx}$  and off-diagonal part  $\sigma_{xy}$  of the optical conductivity of single-layer TMDs (e.g. MoS<sub>2</sub> here) resolved for different valleys and different spins. Panel (a) represents the semiconducting equilibrium case, panel (b) the non-equilibrium case induced by a left-circularly polarized pumping tuned at the  $\omega = \Delta_A$  frequency, which acts only on the top valence band at the K point. Blue and red lines represent contributions from spin up and down, respectively, whereas black lines the total optical conductivity summed up over spin and valleys.

spin  $\uparrow$ . Since only one valley, with a given spin, will be populated in both the valence and conduction band, the photoinduced charge density can be further parametrized in terms of a characteristic momentum  $\bar{p}$ , for which  $f[\epsilon_{0,\sigma}(p)] = 1$ ,  $f[\epsilon_{B,\sigma}(p)] = 0$  ( $p \leq \bar{p}$ ), obeying the relation:

$$n_{\text{pump}} = \frac{\bar{p}^2}{4\pi}. \quad (43)$$

Typical values of  $n_{\text{pump}}$  can range up to  $n_{\text{pump}} \lesssim 0.01/V_{\text{cell}}$ . For a representative case  $n_{\text{pump}} = 0.002/V_{\text{cell}}$ , we get for MoS<sub>2</sub>  $\bar{p}a \approx 0.171$ , and, using  $a = 3.16 \text{ \AA}$ ,  $\bar{p} \approx 0.054 \text{ \AA}^{-1}$ .

Due to the selection rules, only the states at K point with the proper chirality, corresponding in this case to spin up, are affected by the pumping. For  $|p| \leq \bar{p}$  we have thus a *reverse* Pauli blocking. The contribution of these states to the optical conductivity reads thus:

$$\text{Re}\sigma_{xx,\uparrow,\text{pump}}^{0/B}(\omega, \text{K}) = \sigma_0 \frac{v_{0/B}^2}{c_A \hbar \omega} [-\theta(\hbar\omega - \Delta_A) + 2\theta(\hbar\omega - \Delta_A - E_{PA})], \quad (44)$$

$$\text{Im}\sigma_{xy,\uparrow,\text{pump}}^{0/B}(\omega, \text{K}) = -\sigma_0 \frac{v_{0/B}^2}{c_A \hbar \omega} [-\theta(\hbar\omega - \Delta_A) + 2\theta(\hbar\omega - \Delta_A - E_{PA})], \quad (45)$$



where  $E_{P,A} = c_A(\bar{p}a)^2 = 4\pi c_A a^2 n_{\text{pump}}$ . In Fig. 2b we show the effect of the left-circularly polarized pumping on the diagonal and off-diagonal parts of the optical conductivity,  $\sigma_{ij,\text{pump}}(\omega) = \sum_{\sigma,\nu} \sigma'_{xx,\sigma,\text{pump}}(\omega, \nu)$ . Due to the reverse Pauli blocking, the real part of the diagonal term  $\text{Re}\sigma_{xx,\text{pump}}(\omega)$  shows a depletion of spectral intensity close to the A-edge energy. In real samples, in the presence of many-body exciton binding, this depletion appears as a reduction of the A-exciton intensity, as been experimentally observed many times in reflectivity probes. More striking is the result on the off-diagonal component of the optical tensor  $\sigma_{xy,\text{pump}}(\omega)$  where the contributions from spin-up and spin-down transitions and from K and K' close to the A-resonance do not cancel out anymore, giving rise to a *finite* off-diagonal term  $\sigma_{xy,\text{pump}}(\omega) \neq 0$ ,

$$\text{Im}\sigma_{xy,\text{pump}}^{0/B}(\omega) = \sigma_0 \frac{2v_{0/B}^2}{c_A \hbar \omega} [\theta(\hbar\omega - \Delta_A) - \theta(\hbar\omega - \Delta_A - E_{P,A})]. \quad (46)$$

On the experimental ground, the onset of a finite off-diagonal component  $\sigma_{xy,\text{pump}}(\omega) \neq 0$  is observed as an optical (Faraday or Kerr) rotation of the transmitted/reflected polarization of the probe, which commonly signals the presence of a finite effective magnetic field [37–39]. More in details, we estimate a off-diagonal spectral intensity at the A-exciton energy range:

$$I_A = \int_{\Omega_A} d\omega \text{Im}\sigma_{xy,\text{pump}}^{0/B}(\omega) = \sigma_0 \frac{v_{0/B}^2}{\hbar c_A \Delta_A} 2E_{P,A} = 4\pi a^2 \sigma_0 \frac{v_{0/B}^2}{\hbar \Delta_A} 2n_{\text{pump}}, \quad (47)$$

where the spectral off-diagonal intensity is meant to be integrated in a frequency range  $\Omega_A$  close to the A-resonance. We stress here that, although we employ here a non-interacting model to get an analytical insight, the physical origin of such magneto-optical rotation depends uniquely on the selective valley-population enforced by the circularly-polarized pumping, yielding a non-equivalent optical response that does not cancel in the K and K' valleys. This is a quite general mechanism that will not be affected by the formation of localized states when bound excitons form. Within this context, we expect that the step-function spectral shape of Eq. (46), also shown in Fig. 2b, will evolve smoothly in a  $\delta$ -like Lorentzian peak, preserving an integrated intensity  $I_A$  which is dictated by the amount of the spin-polarized photo-induced charges in the conduction and valence bands, and hence still scaling with  $n_{\text{pump}}$ . The onset of a Faraday/Kerr rotation at the A-exciton energy is consistent with previous experimental and theoretical investigations [2,19–23,39]. It is worth underlining here that the valley-selective/spin-selective population induced by the circularly-polarized pumping is expected within our modelling to give rise to a finite pump-driven Kerr/Faraday rotation also at two further energy scales, which we identify with the so-called C-exciton and with another characteristic energy which we denote as D-peak.

We notice a *remarkably strong* band-nesting between these two bands close to the K/K' points. Such feature has been usually disregarded in the context of TMDs, where the analyses have focused on the nesting properties between the valence and the lowest-energy conduction band [56–58]. We relate these transitions with the broad shoulder commonly denoted as C-exciton.

Currently, the origin of the remarkable shoulder in the optical conductivity denoted as C-exciton has not been fully assessed. A mainstream consensus associates this spectral feature with the enhanced optical activity between the valence band and the lowest-energy conduction band along the  $\Gamma$ -K path, where these two bands are thought to have a parallel energy dispersion (*band nesting*) [56–58]. Generalizing this idea within the three-band context, we notice a *remarkably strong* band-nesting at K/K' points between the valence and the lowest-energy conduction, governed by the nesting factor  $\sim 1/|\omega - \epsilon_{T,\sigma}(p) + \epsilon_{B,\sigma}(p)|$ . Prompted by a careful analysis of the first-principle and tight-binding dispersions, we suggest thus a slightly different perspective, where the C-exciton shoulder stems from band-nesting close to the K (K') point between the valence band with  $d_R$  ( $d_L$ ) character and

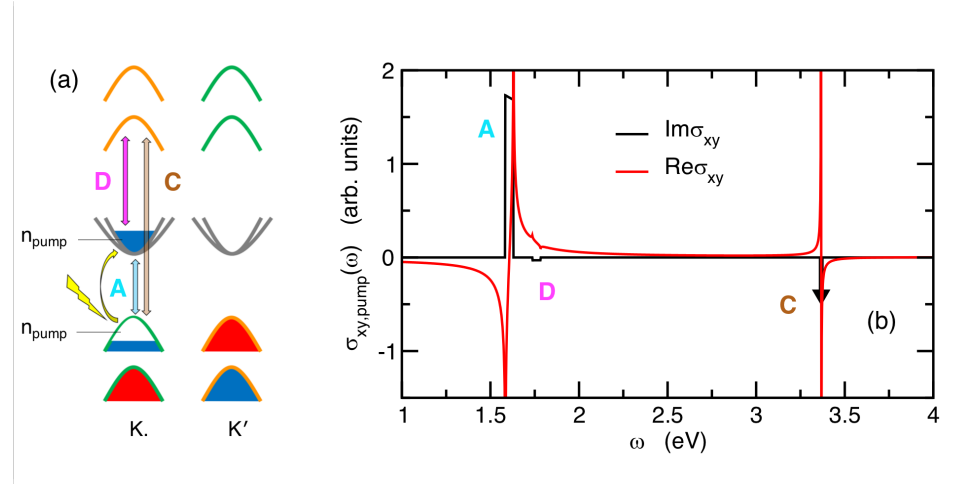


**Figure 3.** (a) Sketch of the optical processes responsible for the Faraday/Kerr rotation at different energies driven by the circularly-polarized pumping, which is parametrized in terms of a charge density  $n_{\text{pump}}$  transferred from the valence to the conduction band at the K point. The vertical light-blue arrow marks the transitions associated with the A-exciton from the valence band with orbital character  $d_R$  to the lowest conduction band with  $d_{3z^2-r^2}$  character. The brown arrow marks the transitions associated with the C-exciton from the valence band with orbital character  $d_R$  to the high-energy conduction band with  $d_L$  character. These processes profit of the strong band-nesting between these two bands close to the K, K' points. The magenta arrow marks the transitions giving rise to an additional optical feature, denoted as D-peak, corresponding to the transitions between lowest conduction band with  $d_{3z^2-r^2}$  character and the high-energy  $d_L$ -band. (b) Real and imaginary part of the off-diagonal component of the optical tensor  $\sigma_{xy,\text{pump}}(\omega)$  as driven by the circularly-polarized pumping. Due to the strong band-nesting, the C-exciton feature in  $\text{Im}\sigma_{xy,\text{pump}}$  is too narrow and sharp to be visible on this scale, and it has been represented by the thick black arrow.

the high-energy conduction band with  $d_L$  ( $d_R$ ) character. In our modelling, neglecting the exciton binding energy, we can expect thus  $\Delta_C = E_T - E_B - 2\lambda$ . Such change of perspective has a deep impact on the predictions about the effects of pumping with circularly-polarized light on the magneto-optical properties. In the original scenario, the  $\mathbf{k}$  points responsible for the band-nesting are located close to the  $\Gamma$  point along the path  $\Gamma$ -K. These states do not have a significant chiral character, as a consequence they have a small spin-splitting and they are weakly entangled with circularly-polarized light. On the contrary, in the present context where band-nesting states lie close to the K, K' points, we can predict a strong chiral character, a different response for spin-up and spin-down charges, a strong entanglement with the circularly-polarized light and a remarkable onset of a off-diagonal component of the optical tensor. Such picture is consistent with the experimental findings observed in Refs. [26,27].

Our three-band model is naturally suited to describe this scenario, where the band-nesting optical transitions responsible for the C-exciton shoulder are accounted by the  $\sigma_{ij,\text{pump}}^{\text{T/B}}(\omega)$  term (see Fig. 3a). At the same time, the photo-induced charging of the conduction band triggers finite optical transitions between the conduction band itself with  $d_{3z^2-r^2}$  and the high-energy conduction band with  $d_L$  ( $d_R$ ) character. The valley-population of these states is also very sensitive to circularly-polarized light, and they are expected thus to drive a finite optical rotation at typical energy, neglecting the exciton binding energy,  $\Delta_D = E_T - E_0 - \lambda = \Delta_C - \Delta_A$  (Fig. 3a). These latter optical transitions are taken into account by the term  $\sigma_{ij,\text{pump}}^{0/\text{T}}(\omega)$ .

The effect of photo-induced pump charging with circularly polarized light in the whole frequency domain can be thus evaluated by considering all the possible contributions,  $\sigma_{ij,\text{pump}}(\omega) = \sigma_{ij,\text{pump}}^{0/\text{B}}(\omega) + \sigma_{ij,\text{pump}}^{\text{T/B}}(\omega) + \sigma_{ij,\text{pump}}^{0/\text{T}}(\omega)$ . The formal structure of each term

is very similar to the term  $\sigma_{ij,\text{pump}}^{0/B}(\omega)$  which we have explicitly evaluated above. Taking into account the slight differences for each term, we get thus:

$$\begin{aligned} \text{Im}\sigma_{xy,\text{pump}}(\omega) &= \sigma_0 \frac{2v_{0/B}^2}{c_A \hbar \omega} [\theta(\hbar\omega - \Delta_A) - \theta(\hbar\omega - \Delta_A - E_{P,A})] \\ &\quad - \sigma_0 \frac{v_{T/B}^2}{|c_C| \hbar \omega} [\theta(\hbar\omega - \Delta_C) - \theta(\hbar\omega - \Delta_C - E_{P,C})] \\ &\quad - \sigma_0 \frac{v_{0/T}^2}{|c_D| \hbar \omega} [\theta(\hbar\omega - \Delta + E_{P,D}) - \theta(\hbar\omega - \Delta_D)], \end{aligned} \quad (48)$$

where

$$c_C = \bar{a}_{T,\uparrow} - \bar{a}_{B,\uparrow}, \quad (49)$$

$$c_D = \bar{a}_{T,\uparrow} - \bar{a}_{0,\uparrow}, \quad (50)$$

and where  $E_{P,C} = |c_C|(\bar{p}a)^2 = 4\pi|c_C|a^2n_{\text{pump}}$ ,  $E_{P,D} = |c_D|(\bar{p}a)^2 = 4\pi|c_D|a^2n_{\text{pump}}$ . The real part  $\text{Re}\sigma_{xy,\text{pump}}(\omega)$  is thus obtained by Kramers-Kronig relations. In Eq. (48) we have assumed that  $c_C > 0$ , which is a valid assumption for the W-based transition-metal dichalcogenides  $\text{WS}_2$ ,  $\text{WSe}_2$ ,  $\text{WTe}_2$  (see Table A1). However, since these materials are very close to the perfect band-nesting limit ( $c_C \approx 0$ ) for these states at the K, K' point, the sign of  $c_C$  is not *a priori* determined. For the  $\text{MoX}_2$  family for instance  $c_C < 0$  (see Table A1), and the analytical expression  $\text{Im}\sigma_{xy,\text{pump}}(\omega)$  should rather read:

$$\begin{aligned} \text{Im}\sigma_{xy,\text{pump}}(\omega) &= \sigma_0 \frac{2v_{0/B}^2}{c_A \hbar \omega} [\theta(\hbar\omega - \Delta_A) - \theta(\hbar\omega - \Delta_A - E_{P,A})] \\ &\quad - \sigma_0 \frac{v_{T/B}^2}{|c_C| \hbar \omega} [\theta(\hbar\omega - \Delta_C + E_{P,C}) - \theta(\hbar\omega - \Delta_C)] \\ &\quad - \sigma_0 \frac{v_{0/T}^2}{|c_D| \hbar \omega} [\theta(\hbar\omega - \Delta + E_{P,D}) - \theta(\hbar\omega - \Delta_D)]. \end{aligned} \quad (51)$$

The plot of  $\sigma_{xy,\text{pump}}(\omega)$  for  $\text{MoS}_2$ , with a pump-driven photo-induced charge density  $n_{\text{pump}} = 0.002/V_{\text{cell}}$  ( $\bar{p}a \approx 0.171$ ) is shown in Fig. 3b, showing how a valley-selective population due to a circularly-polarized pumping gives rise to a finite off-diagonal component (and hence to a finite Farady/Kerr effect) not only at the A-exciton energy  $\Delta_A$ , but also at the C-exciton energy  $\Delta_C$  and at another energy range  $\Delta_D$  corresponding to  $\Delta_D \approx \Delta_C - \Delta_A$ , net of the exciton binding energy. We predict thus an opposite sign of off-diagonal component of the optical tensor (and hence an opposite Farady/Kerr rotation) at the energies  $\Delta_C$ ,  $\Delta_D$  compared with the one predicted at the A-exciton energy scale. The absolute intensity of these additional features in the off-diagonal component of the optical tensor is found:

$$I_C = \sigma_0 \frac{v_{T/B}^2}{\hbar c_C \Delta_C} E_{P,C} = 4\pi a^2 \sigma_0 \frac{v_{T/B}^2}{\hbar \Delta_C} n_{\text{pump}}, \quad (52)$$

$$I_D = \sigma_0 \frac{v_{0/T}^2}{\hbar c_D \Delta_D} E_{P,D} = 4\pi a^2 \sigma_0 \frac{v_{0/T}^2}{\hbar \Delta_D} n_{\text{pump}}. \quad (53)$$

The expression of Eqs (52), (53) is formally identical at Eq. (47) for  $I_A$ , upon changing the proper variables, with the noticeable difference of a factor 2. This is due to the fact that the strength of  $\sigma_{xy,\text{pump}}(\omega)$  at  $\omega \approx \Delta_A$  profits of the presence of the pump-driven charge in *both* the conduction and valence bands. On the other hand, the onset of a finite off-diagonal component  $\sigma_{xy,\text{pump}}(\omega)$  at the energies  $\omega \approx \Delta_C$ ,  $\omega \approx \Delta_D$  is related in an independent way only to the pump-driven charge in the conduction band and in the valence band,

respectively. This complex multi-peak structure of the pump-induced Faraday/Kerr effect opens interesting perspective not only for characterizing and proving the onset of these effects, but also for harvesting them for multi-frequency operative devices.

### 5. Time-dependence

In the previous Section we have shown, using an appropriate three-band model, how a valley-selective population driven by a circularly-polarized pump can give rise to an off-diagonal component of the optical tensor, and hence to a finite Faraday/Kerr optical rotation at *three* characteristic energies, related to the A-exciton, the C-exciton, and to another energy scale governed by the optical transitions between the lowest conduction band and high-energy conduction band, roughly determined by the energy difference between the A and C-exciton.

Most notable, in this description, is the absence of any Faraday/Kerr signature at the B-exciton energy. This is essentially due to the strong light-polarization/orbital/valley/spin entanglement, so that a circularly-polarized pumping tuned at the A-exciton resonance induces valley/spin selective population. More in particular, a left-circularly polarized light tuned at the A-exciton resonance, in the absence of scattering, triggers particle-hole transitions uniquely at the K valley and uniquely for spin-up electrons, making thus an optical unbalance only in the spin-up sector. This scenario gives rise to a finite Faraday/Kerr signature only close to the energies  $\omega \approx \Delta_A$ ,  $\omega \approx \Delta_C$ ,  $\omega \approx \Delta_D$ . Such snapshot is valid however only on a short time-scale, before impurity and many-body scattering can cause spin-flip and/or intervalley processes.

In order to gain an insight about how these many-body scattering can affect the magneto-optical Faraday/Kerr properties induced by a circularly-polarized pumping, we consider the charge density in each relevant band which is involved in the time-dynamics. We denote thus  $n_{3z^2-r^2,\sigma}(\nu)$  the charge density in the lowest-energy conduction band with  $d_{3z^2-r^2}$ -orbital and  $\sigma$ -spin character at the  $\nu$  valley,  $n_{R,\uparrow}(\mathbf{K})$  the charge (hole) density in the valence band at the K valley with spin-up, and  $n_{L,\downarrow}(\mathbf{K}')$  the charge (hole) density in the valence band at the  $\mathbf{K}'$  valley with spin-down. Neglecting the frequency-resolved details of each optical feature, we can estimate the ‘‘Faraday/Kerr’’ intensity of each spectral feature as:

$$I_A(t) \approx n_{3z^2-r^2,\uparrow}(\mathbf{K},t) + n_{R,\uparrow}(\mathbf{K},t) - n_{3z^2-r^2,\downarrow}(\mathbf{K}',t) - n_{L,\downarrow}(\mathbf{K}',t), \quad (54)$$

$$I_C(t) \approx n_{R,\uparrow}(\mathbf{K},t) - n_{L,\downarrow}(\mathbf{K}',t), \quad (55)$$

$$I_D(t) \approx n_{3z^2-r^2,\uparrow}(\mathbf{K},t) - n_{3z^2-r^2,\downarrow}(\mathbf{K}',t), \quad (56)$$

$$I_B(t) \approx n_{3z^2-r^2,\downarrow}(\mathbf{K},t) - n_{3z^2-r^2,\uparrow}(\mathbf{K}',t). \quad (57)$$

Here following the analysis for the other features, we have properly estimated the intensity of a spectral feature at the energy corresponding to the B-exciton as resulting by the  $d_{R,\downarrow}(\mathbf{K}) \leftrightarrow d_{3z^2-r^2,\downarrow}(\mathbf{K})$  and  $d_{L,\uparrow}(\mathbf{K}') \leftrightarrow d_{3z^2-r^2,\uparrow}(\mathbf{K}')$ , and hence governed by the time-dynamics of  $n_{3z^2-r^2,\downarrow}(\mathbf{K})$  and  $n_{3z^2-r^2,\uparrow}(\mathbf{K}')$ . In all the cases, we have taken into account that, due to the orbital/spin/valley entanglement, similar processes at  $\mathbf{K}'$  cancel the contributions at the K valley. Assuming an initial pumping with left-circularly polarized photons resonant at the A-exciton energy, we model at  $t = 0$  the respective charge density as:  $n_{3z^2-r^2,\uparrow}(\mathbf{K},0) = n_{R,\uparrow}(\mathbf{K},0) = n_{\text{pump}}$ ,  $n_{3z^2-r^2,\downarrow}(\mathbf{K},0) = n_{3z^2-r^2,\downarrow}(\mathbf{K}',0) = n_{3z^2-r^2,\uparrow}(\mathbf{K}',0) = n_{L,\downarrow}(\mathbf{K}',0) = 0$ . These conditions reproduce the static results discussed in the previous Section.

Recombination processes, related to annihilation of particle-hole excitations, are known to occur on a very long time scale. On the other hand, the off-diagonal term  $\sigma_{xy,\text{pump}}(\omega)$  of the optical tensor is expected to vanish on a much shorter time scale when scattering processes redistribute the charge in both the conduction and valence bands giving identical populations in the K,  $\mathbf{K}'$  valley. Neglecting the very weak intravalley spin-flip processes, two main scattering channels have been identified in this scenario [16,34–36,59–61]: (i) an interband spin-conserving scattering, mediated by electron-phonon

coupling and/or impurities, where the charge-density of the conduction band with given spin is scattered for a valley  $\nu$  to the opposite valley  $-\nu$ . This process is hampered in the valence band due to the spin-splitting [34,36,61]; (ii) spin-flip intervalley exchange where a particle-hole couple in a given valley with given spin is scattered into the opposite valley with reverse spin [36,60,62]. According with this picture, we model in a compact way the time dynamics of the pump-driven charges with a set of coupled equations:

$$\frac{dn_{3z^2-r^2,\uparrow}(\mathbf{K})}{dt} = \alpha f(t) - \frac{\min[n_{3z^2-r^2,\uparrow}(\mathbf{K}), n_{\mathbf{R},\uparrow}(\mathbf{K})] - \min[n_{3z^2-r^2,\downarrow}(\mathbf{K}'), n_{\mathbf{L},\downarrow}(\mathbf{K}')]}{\tau_{\text{exc}}} - \frac{n_{3z^2-r^2,\uparrow}(\mathbf{K}) - n_{3z^2-r^2,\uparrow}(\mathbf{K}')}{\tau_0}, \quad (58)$$

$$\frac{dn_{3z^2-r^2,\downarrow}(\mathbf{K})}{dt} = -\frac{n_{3z^2-r^2,\downarrow}(\mathbf{K}) - n_{3z^2-r^2,\downarrow}(\mathbf{K}')}{\tau_0}, \quad (59)$$

$$\frac{dn_{\mathbf{R},\uparrow}(\mathbf{K})}{dt} = \alpha f(t) - \frac{\min[n_{3z^2-r^2,\uparrow}(\mathbf{K}), n_{\mathbf{R},\uparrow}(\mathbf{K})] - \min[n_{3z^2-r^2,\downarrow}(\mathbf{K}'), n_{\mathbf{L},\downarrow}(\mathbf{K}')]}{\tau_{\text{exc}}} \quad (60)$$

$$\frac{dn_{3z^2-r^2,\uparrow}(\mathbf{K}')}{dt} = -\frac{n_{3z^2-r^2,\uparrow}(\mathbf{K}') - n_{3z^2-r^2,\uparrow}(\mathbf{K})}{\tau_0}, \quad (61)$$

$$\frac{dn_{3z^2-r^2,\downarrow}(\mathbf{K}')}{dt} = -\frac{\min[n_{3z^2-r^2,\downarrow}(\mathbf{K}'), n_{\mathbf{L},\downarrow}(\mathbf{K}')] - \min[\min[n_{3z^2-r^2,\uparrow}(\mathbf{K}), n_{\mathbf{R},\uparrow}(\mathbf{K})]}{\tau_{\text{exc}}} - \frac{n_{3z^2-r^2,\downarrow}(\mathbf{K}') - n_{3z^2-r^2,\downarrow}(\mathbf{K})}{\tau_0}, \quad (62)$$

$$\frac{dn_{\mathbf{L},\downarrow}(\mathbf{K}')}{dt} = -\frac{\min[n_{3z^2-r^2,\downarrow}(\mathbf{K}'), n_{\mathbf{L},\downarrow}(\mathbf{K}')] - \min[\min[n_{3z^2-r^2,\uparrow}(\mathbf{K}), n_{\mathbf{R},\uparrow}(\mathbf{K})]}{\tau_{\text{exc}}}, \quad (63)$$

where  $f(t)$  is the profile of the pump pulse,  $\alpha$  is related to the absorption coefficient, and  $\tau_{\text{exc}}$ ,  $\tau_0$  are the scattering rates of the two processes discussed above. The factors  $\min[n_{3z^2-r^2,\uparrow}(\mathbf{K}), n_{\mathbf{R},\uparrow}(\mathbf{K})]$  and  $\min[n_{3z^2-r^2,\downarrow}(\mathbf{K}'), n_{\mathbf{L},\downarrow}(\mathbf{K}')]$  take into account that the intervalley exchange scattering requires the presence of both particle-hole changes in the conduction and valence bands. We take in the following representative values  $\tau_0 = 200$  fs [35,63] and  $\tau_{\text{exc}} = 1.8$  ps [20,62]. The time dynamics of the different charge densities  $n_{i,\sigma}(\nu)$  is shown in Fig. 4a, and the corresponding time-dependence of the Kerr intensity of the different spectral features in Fig. 4b, whereas panel (c) depicts some representative time-snapshots of  $n_{i,\sigma}(\nu)$ . Notice that, in order to focus on the time dynamics, we plot here only the dependence of  $I_\mu(t)$  on the time-dependent charge densities  $n_{i,\sigma}(\nu, t)$ , neglecting the current operator matrix elements and other time-independent factors, so that the relative ratio of the intensities here is not meant to be representative of the experimental ratio. The overall behavior of  $n_{i,\sigma}(\nu)$  and  $I_A(t)$  that we get is in very good agreement with the results by Ref. [36], performed with *ab-initio* techniques.

We can identify there three main regimes: (i) a short-time scale  $t \ll \tau_0$  (grey areas, left panel of Fig. 4c) where the charge populations are mainly determined by the driving pump, with a significant population of only  $n_{3z^2-r^2,\uparrow}(\mathbf{K})$  and  $n_{\mathbf{R},\uparrow}(\mathbf{K})$ . This is reflected in a sharp onset of the Farady/Kerr intensities  $I_A(t)$ ,  $I_C(t)$  and  $I_D(t)$ . (ii) soon after this scenario, in the short time-range  $t \sim \tau_0$  (yellow areas, middle panel of Fig. 4c), the impurity/electron-phonon scattering has a main effect of a depletion of  $n_{3z^2-r^2,\uparrow}(\mathbf{K})$  due a redistribution of the spin-up conduction electrons towards  $n_{3z^2-r^2,\uparrow}(\mathbf{K}')$ . As a consequence, a sharp decrease of  $I_A(t) \propto e^{-t/2\tau_0}$  and  $I_D(t) \propto e^{-t/2\tau_0}$  is predicted, whereas the finite valley population  $n_{3z^2-r^2,\uparrow}(\mathbf{K}')$  gives rise to a finite (delayed) intensity of  $I_B(t)$ . (iii) in a following time regime  $\tau_0 \ll t \sim \tau_{\text{exc}}$  (light blue areas, right panel of Fig. 4c) the key many-body process is the exchange scattering (assisted by the impurity/electron-phonon one) leading towards a slower equal spin population of each conduction and valence band. The total spectral intensities in this regime scale as  $I_\mu(t) \propto e^{-t/2\tau_{\text{exc}}}$ . The final steady state (right panel of Fig. 4c) is however reached only for  $t \gg \tau_{\text{exc}}$ . In this regime the

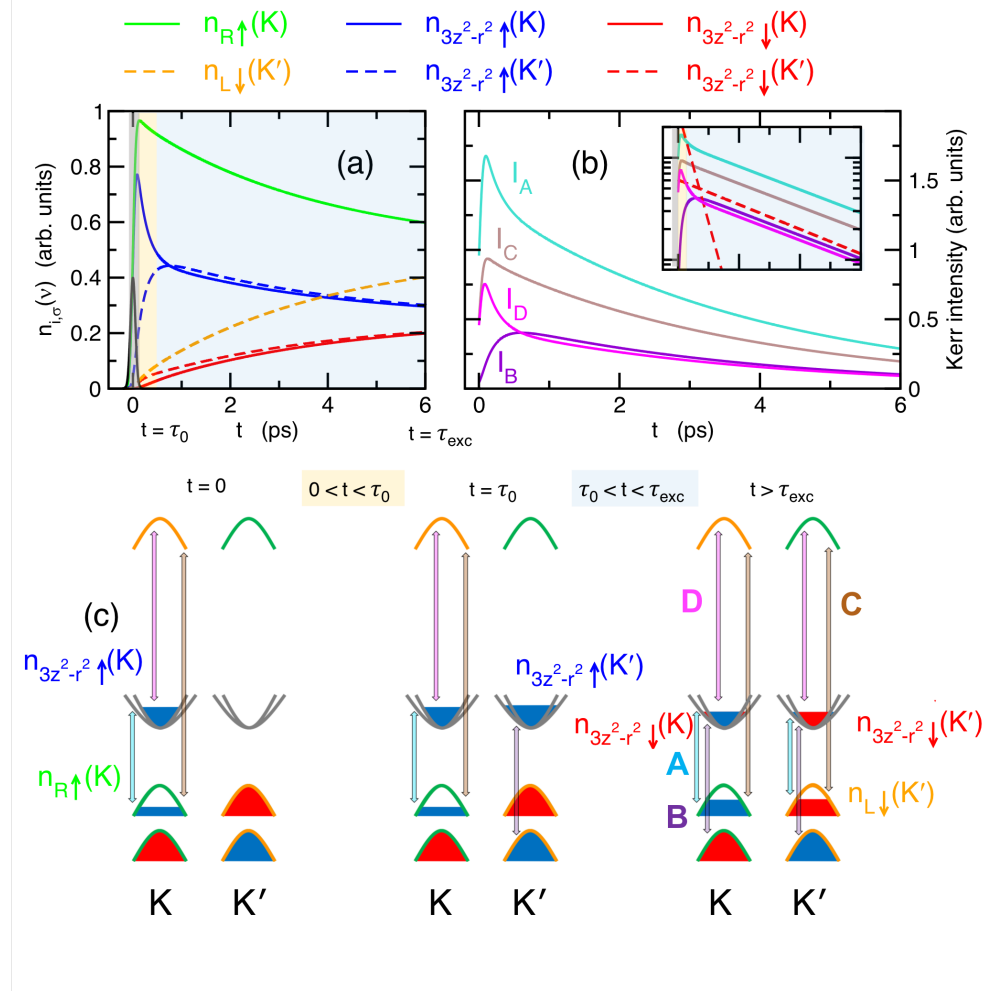


**Figure 4.** (a) Time-dependence of the pump-driven charge densities  $n_{i,\sigma}(v)$  upon a Gaussian pump with width  $\sim 50$  fs (black solid line). Legend for different charge densities is reported above. (b) Corresponding time-dependence of the integrated Faraday/Kerr intensities of the different spectral features associated with different optical interband transitions. Inset: the same on a linear-log plot, where the red dashed lines represent the exponential behaviors decay rate  $2\tau_0$  and  $2\tau_{exc}$  respectively. (c) Sketch of the spin-resolved charge densities  $n_{i,\sigma}(v)$  in the conduction and valence bands at the K and K' points along with the main optical transitions in the different time regimes as outlined in the panels above.

contributions of off-diagonal elements of the optical tensor at K and K' cancel out, and any Faraday/Kerr effect vanishes. Note that the transient Faraday/Kerr intensity at the B-exciton energy range is a by-product of the finite valley-K' population of  $n_{3z^2-r^2,\uparrow}$ . In similar way as this valley-transient population is expected to give rise to a Faraday/Kerr effect at the energy  $\Delta_B$  associated with optical transitions between  $n_{L,\uparrow}(K')$  and  $n_{3z^2-r^2,\uparrow}(K')$ , we can expect the appearance of further Faraday/Kerr features at the energies associated with optical transitions between  $n_{L,\uparrow}(K')$  and  $n_{R,\uparrow}(K')$  and between  $n_{3z^2-r^2,\uparrow}(K')$  and  $n_{R,\uparrow}(K')$ . We denote these transitions as  $\Delta'_C$  and  $\Delta'_D$ , whose Faraday/Kerr spectral intensity scales, assuming pumping tuned at the A-exciton resonance, as  $I'_C(t) \propto I_C(t)$  and  $I'_D(t) \propto I_D(t)$ . The band-parameters determining the detailed spectral properties of these features are also listed in Table A1.



## 6. Conclusions

In summary, in the present paper we have addressed in an analytical way the onset of a finite Faraday/Kerr effect in single-layer transition-metal dichalcogenides upon pumping with a circularly polarized light at the A-resonance. To this aim we have introduced a proper three-band analytical  $\mathbf{k} \cdot \mathbf{p}$  model that retains all the orbital complexity of original band-structure and of the optical selection rules. We have shown how a pump-driven spin/valley selective population gives rise to a finite off-diagonal component of the optical tensor responsible for different spectral features in the Faraday/Kerr optical rotation. We recover the signature of a Faraday/Kerr rotation in the proximity of pump energy at the A-exciton resonance, in accordance with the available experimental and theoretical findings [2,19–23,39], and we predict the onset of a Faraday/Kerr signal at the C-exciton resonance and at a further energy scale related to the high-energy conduction band. These predictions can guide future experimental investigation, spanning also the different families of  $MX_2$  TMDs. We have further modelled the effects of time-dynamics driven by the many-body scattering, and the consequent emerging of additional transient Faraday/Kerr optical features. Our results provide a suitable compact modelling for describing the magneto-optical properties induced in transition-metal dichalcogenides by circularly polarized pumping, in terms of few simple intuitive representative parameters.

**Funding:** E.C. acknowledges financial support from PNRR MUR Project No. PE0000023-NQSTI.

**Acknowledgments:**

**Conflicts of Interest:** The authors declare no conflicts of interest.

## Appendix A Mapping $\mathbf{k} \cdot \mathbf{p}$ band parameters in terms of TB parameters

Below we summarized useful analytical expressions for the band-parameters of the  $\mathbf{k} \cdot \mathbf{p}$  Hamiltonian in Eqs. (6)-(7) in terms of the original tight-binding parameters provided in Ref. [54].

We have explicitly:

$$E_0 = \epsilon_1 - 3(t_0 - 2r_0 + u_0), \quad (\text{A1})$$

$$E_T = \epsilon_2 - \frac{3}{2}(t_{11} + t_{22} - 4r_{11} + u_{11} + u_{22}) + 2\sqrt{3}r_{12} + 3\sqrt{3}t_{12} - 3\sqrt{3}u_{12}, \quad (\text{A2})$$

$$E_B = \epsilon_2 - \frac{3}{2}(t_{11} + t_{22} - 4r_{11} + u_{11} + u_{22}) + 2\sqrt{3}r_{12} - 3\sqrt{3}t_{12} + 3\sqrt{3}u_{12}, \quad (\text{A3})$$

$$a_0 = \frac{3(t_0 - 6r_0 + 4u_0)}{4}, \quad (\text{A4})$$

$$a_T = \frac{3}{8}(t_{11} + 4u_{11} + t_{22} + 4u_{22}) - \frac{9}{2}r_{11} - \frac{3\sqrt{3}}{2}r_{12} - \frac{3\sqrt{3}}{4}t_{12} + 3\sqrt{3}u_{12}, \quad (\text{A5})$$

$$a_B = \frac{3}{8}(t_{11} + 4u_{11} + t_{22} + 4u_{22}) - \frac{9}{2}r_{11} - \frac{3\sqrt{3}}{2}r_{12} + \frac{3\sqrt{3}}{4}t_{12} - 3\sqrt{3}u_{12}, \quad (\text{A6})$$

$$v_{0/T} = -\frac{3\sqrt{3}}{2\sqrt{2}}t_2 + \frac{3\sqrt{3}}{\sqrt{2}}u_2 + \frac{3}{2\sqrt{2}}t_1 - \frac{3(r_1 - r_2)}{\sqrt{2}} + \frac{3}{\sqrt{2}}u_1, \quad (\text{A7})$$

$$v_{0/B} = -\frac{3\sqrt{3}}{2\sqrt{2}}t_2 + \frac{3\sqrt{3}}{\sqrt{2}}u_2 - \frac{3}{2\sqrt{2}}t_1 + \frac{3(r_1 - r_2)}{\sqrt{2}} - \frac{3}{\sqrt{2}}u_1, \quad (\text{A8})$$

$$v_{T/B} = \frac{3\sqrt{3}}{4}(t_{11} - t_{22} - 2u_{11} + 2u_{22}). \quad (\text{A9})$$

The terms  $\bar{a}_{T,\sigma}$ ,  $\bar{a}_{0,\sigma}$ ,  $\bar{a}_{B,\sigma}$  are related to the dispersion mass of each band, and they are obtained within the  $\mathbf{k} \cdot \mathbf{p}$  context as:

$$\bar{a}_{T,\uparrow} = a_T p^2 + \gamma_{T/B,\uparrow} + \gamma_{T/0,\uparrow}, \quad (\text{A10})$$

$$\bar{a}_{0,\uparrow} = a_0 + \gamma_{0/B,\uparrow} - \gamma_{T/0,\uparrow}, \quad (\text{A11})$$

$$\bar{a}_{B,\uparrow} = a_B p - \gamma_{T/B,\uparrow} - \gamma_{0/B,\uparrow}, \quad (\text{A12})$$

$$\bar{a}_{T,\downarrow} = a_T p^2 + \gamma_{T/B,\downarrow} + \gamma_{T/0,\downarrow}, \quad (\text{A13})$$

$$\bar{a}_{0,\downarrow} = a_0 + \gamma_{0/B,\downarrow} - \gamma_{T/0,\downarrow}, \quad (\text{A14})$$

$$\bar{a}_{B,\downarrow} = a_B p - \gamma_{T/B,\downarrow} - \gamma_{0/B,\downarrow}, \quad (\text{A15})$$

and where

$$\gamma_{T/B,\sigma} = \frac{v_{T/B}^2}{E_T - E_B + 2\lambda I_\sigma}, \quad (\text{A16})$$

$$\gamma_{T/0,\sigma} = \frac{v_{0/T}^2}{E_T - E_0 + \lambda I_\sigma}, \quad (\text{A17})$$

$$\gamma_{0/B,\sigma} = \frac{v_{0/B}^2}{E_0 - E_B + \lambda I_\sigma}. \quad (\text{A18})$$

The spin-dependent single-particle energies at the K point read thus:

$$\epsilon_{T,\uparrow} = E_T - \lambda, \quad (\text{A19})$$

$$\epsilon_{0,\uparrow} = E_0, \quad (\text{A20})$$

$$\epsilon_{B,\uparrow} = E_B + \lambda, \quad (\text{A21})$$

$$\epsilon_{T,\downarrow} = E_T + \lambda, \quad (\text{A22})$$

$$\epsilon_{0,\downarrow} = E_0, \quad (\text{A23})$$

$$\epsilon_{B,\downarrow} = E_B - \lambda, \quad (\text{A24})$$

and the characteristic interband optical edges:

$$\Delta_A = \epsilon_{0,\uparrow} - \epsilon_{B,\uparrow}, \quad (\text{A25})$$

$$\Delta_B = \epsilon_{0,\downarrow} - \epsilon_{B,\downarrow}, \quad (\text{A26})$$

$$\Delta_C = \epsilon_{T,\uparrow} - \epsilon_{B,\uparrow}, \quad (\text{A27})$$

$$\Delta_D = \epsilon_{T,\uparrow} - \epsilon_{0,\uparrow}, \quad (\text{A28})$$

$$\Delta_{C'} = \epsilon_{T,\downarrow} - \epsilon_{B,\downarrow}, \quad (\text{A29})$$

$$\Delta_{D'} = \epsilon_{T,\downarrow} - \epsilon_{0,\downarrow}. \quad (\text{A30})$$

In Table A1 we summarize the numerical values of our three-band  $\mathbf{k} \cdot \mathbf{p}$  model obtained from the initial tight-binding parameters of Ref. [54]:

## References

1. Jariwala, D. and Sangwan, V.K. and Lauhon, L.J. and Marks, T.J. and Hersam, M.C.. Emerging Device Applications for Semiconducting Two-Dimensional Transition Metal Dichalcogenides. *ACS Nano* **2014**, *8*, 1102–1120. <https://doi.org/10.1021/nn500064s>.
2. Sun, Z.P. and Martinez, A. and Wang, F.. Optical modulators with 2D layered materials. *Nat. Photon.* **2016**, *10*, 227–238. <https://doi.org/10.1038/NPHOTON.2016.15>.
3. Manzeli, S.; Ovchinnikov, D.; Pasquier, D.; Yazyev, O.V.; Kis, A. 2D transition metal dichalcogenides. *Nat. Rev. Materials* **2017**, *2*, 17033. <https://doi.org/10.1038/natrevmats.2017.33>.
4. Arora, Ashish. Magneto-optics of layered two-dimensional semiconductors and heterostructures: Progress and prospects. *Journal of Applied Physics* **2021**, *129*, 120902. <https://doi.org/10.1063/5.0042683>.
5. Mak, K.Fai and Lee, Ch. and Hone, J. and Shan, J. and Heinz, T.F.. Atomically Thin MoS<sub>2</sub>: A New Direct-Gap Semiconductor. *Phys. Rev. Lett.* **2010**, *105*, 136805. <https://doi.org/10.1103/PhysRevLett.105.136805>.



**Table A1.** This is a table caption.

|                           | MoS <sub>2</sub> | MoSe <sub>2</sub> | MoTe <sub>2</sub> | WS <sub>2</sub> | WSe <sub>2</sub> | WTe <sub>2</sub> |
|---------------------------|------------------|-------------------|-------------------|-----------------|------------------|------------------|
| $\lambda$                 | 0.073            | 0.091             | 0.107             | 0.211           | 0.228            | 0.237            |
| $E_T$                     | 3.451            | 3.056             | 2.525             | 3.933           | 3.443            | 2.871            |
| $E_0$                     | 1.595            | 1.482             | 1.113             | 1.749           | 1.565            | 1.132            |
| $E_B$                     | -0.062           | 0.053             | 0.041             | -0.057          | 0.024            | 0.065            |
| $\epsilon_{T,\uparrow}$   | 3.378            | 2.965             | 2.418             | 3.722           | 3.215            | 2.634            |
| $\epsilon_{0,\uparrow}$   | 1.595            | 1.482             | 1.113             | 1.749           | 1.565            | 1.132            |
| $\epsilon_{B,\uparrow}$   | 0.011            | 0.144             | 0.148             | 0.154           | 0.252            | 0.302            |
| $\epsilon_{T,\downarrow}$ | 3.524            | 3.147             | 2.632             | 4.144           | 3.671            | 3.108            |
| $\epsilon_{0,\downarrow}$ | 1.595            | 1.482             | 1.113             | 1.749           | 1.565            | 1.132            |
| $\epsilon_{B,\downarrow}$ | -0.135           | -0.038            | -0.066            | -0.268          | -0.204           | -0.172           |
| $\Delta_A$                | 1.584            | 1.338             | 0.965             | 1.595           | 1.313            | 0.830            |
| $\Delta_B$                | 1.730            | 1.520             | 1.179             | 2.017           | 1.769            | 1.304            |
| $\Delta_C$                | 3.367            | 2.821             | 2.270             | 3.569           | 2.963            | 2.332            |
| $\Delta_D$                | 1.783            | 1.483             | 1.305             | 1.973           | 1.650            | 1.502            |
| $\Delta_{C'}$             | 3.659            | 3.185             | 2.698             | 4.413           | 3.875            | 3.280            |
| $\Delta_{D'}$             | 1.929            | 1.665             | 1.519             | 2.395           | 2.106            | 1.976            |
| $a_T$                     | -1.190           | -1.170            | -1.142            | -1.305          | -1.310           | -1.221           |
| $a_0$                     | -0.493           | -0.411            | -0.012            | -0.586          | -0.455           | -0.212           |
| $a_B$                     | 1.060            | 0.921             | 0.578             | 1.299           | 1.119            | 0.860            |
| $\bar{a}_{T,\uparrow}$    | -0.800           | -0.774            | -0.768            | -0.836          | -0.829           | -0.816           |
| $\bar{a}_{0,\uparrow}$    | 0.961            | 0.800             | 0.873             | 1.512           | 1.375            | 1.624            |
| $\bar{a}_{B,\uparrow}$    | -0.777           | -0.675            | -0.667            | -1.245          | -1.161           | -1.346           |
| $\bar{a}_{T,\downarrow}$  | -0.831           | -0.819            | -0.826            | -0.925          | -0.941           | -0.932           |
| $\bar{a}_{0,\downarrow}$  | 0.838            | 0.654             | 0.710             | 1.071           | 0.902            | 0.953            |
| $\bar{a}_{B,\downarrow}$  | -0.637           | -0.505            | -0.470            | -0.756          | -0.628           | -0.615           |
| $v_{0/B}$                 | -1.545           | -1.292            | 0.956             | -1.850          | -1.565           | -1.244           |
| $v_{0/T}$                 | -0.306           | -0.236            | 0.286             | -0.303          | -0.246           | -0.204           |
| $v_{T/B}$                 | -1.065           | -1.001            | 0.841             | -1.228          | -1.148           | -0.938           |
| $c_A$                     | 1.739            | 1.475             | 1.540             | 2.757           | 2.535            | 2.969            |
| $c_B$                     | 1.474            | 1.160             | 1.180             | 1.828           | 1.530            | 1.568            |
| $c_C$                     | -0.023           | -0.098            | -0.101            | 0.409           | 0.332            | 0.530            |
| $c_D$                     | -1.762           | -1.573            | -1.641            | -2.348          | -2.204           | -2.439           |
| $c_{C'}$                  | -0.194           | -0.314            | -0.356            | -0.168          | -0.313           | -0.317           |
| $c_{D'}$                  | -1.669           | -1.473            | -1.536            | -1.996          | -1.843           | -1.884           |

- Sallen, G. and Bouet, L. and Marie, X. and Wang, G. and Zhu, C. R. and Han, W. P. and Lu, Y. and Tan, P. H. and Amand, T. and Liu, B. L. and Urbaszek, B.. Robust optical emission polarization in MoS<sub>2</sub> monolayers through selective valley excitation. *Phys. Rev. B* **2012**, *86*, 081301. <https://doi.org/10.1103/PhysRevB.86.081301>.
- Xiao, D. and Liu, G.-B. and Feng, W. and Xu, X. and Yao, W.. Coupled Spin and Valley Physics in Monolayers of MoS<sub>2</sub> and Other Group-VI Dichalcogenides. *Phys. Rev. Lett.* **2012**, *108*, 196802. <https://doi.org/10.1103/PhysRevLett.108.196802>.
- Zeng, Hualing and Dai, Junfeng and Yao, Wang and Xiao, Di and Cui, Xiaodong. Valley polarization in MoS<sub>2</sub> monolayers by optical pumping. *Nature Nanotechnology* **2012**, *7*, 490–493. <https://doi.org/10.1038/NNANO.2012.95>.
- Wu, Sanfeng and Ross, Jason S. and Liu, Gui-Bin and Aivazian, Grant and Jones, Aaron and Fei, Zaiyao and Zhu, Wenguang and Xiao, Di and Yao, Wang and Cobden, David and Xu, Xiaodong. Electrical tuning of valley magnetic moment through symmetry control in bilayer MoS<sub>2</sub>. *Nature Physics* **2013**, *9*, 149–153. <https://doi.org/10.1038/nphys2524>.
- Liu, Gui-Bin and Xiao, Di and Yao, Yugui and Xu, Xiaodong and Yao, Wang. Electronic structures and theoretical modelling of two-dimensional group-VIB transition metal dichalcogenides. *Chem. Soc. Rev.* **2015**, *44*, 2643–2663. <https://doi.org/10.1039/C4CS00301B>.
- Roldàn, R.; Castellanos-Gomez, A.; Cappelluti, E.; Guinea, F. Strain engineering in semiconducting two-dimensional crystals. *J. Physics: Cond. Matter* **2015**, *27*, 313201. <https://doi.org/10.1088/0953-8984/27/31/313201>.
- Splendiani, A. and Sun, L. and Zhang, Y. and Li, T. and Kim, J. and Chim, C.-Y. and Galli, G. and Wang, F.. Emerging Photoluminescence in Monolayer MoS<sub>2</sub>. *Nano Letters* **2010**, *10*, 1271–1275. <https://doi.org/10.1021/nl903868w>.
- Schaibley, J.R.; Yu, H.; Clark, G.; Rivera, P.; Ross, J.S.; Seyler, K.L.; Yao, W.; Xu, X. Valleytronics in 2D materials. *Nature Reviews Materials* **2016**, *1*, 16055. <https://doi.org/10.1038/natrevmats.2016.55>.
- Liu, Y.; Gao, Y.; Zhang, S.; He, J.; Yu, J.; Liu, Z. Valleytronics in transition metal dichalcogenides materials. *Nano Research* **2019**, *12*, 2695–2711. <https://doi.org/10.1007/s12274-019-2497-2>.

15. Ashish Soni and Suman Kalyan Pal. Valley degree of freedom in two-dimensional van der Waals materials. *Journal of Physics D: Applied Physics* **2022**, *55*, 303003. <https://doi.org/10.1088/1361-6463/ac5bc9>.
16. Mak, Kin Fai and He, Keliang and Shan, Jie and Heinz, Tony F. Control of valley polarization in monolayer MoS<sub>2</sub> by optical helicity. *Nature Nanotechnology* **2012**, *7*, 494–498. <https://doi.org/10.1038/NNANO.2012.96>.
17. Cao, Ting and Wang, Gang and Han, Wenpeng and Ye, Huiqi and Zhu, Chuanrui and Shi, Junren and Niu, Qian and Tan, Pingheng and Wang, Enge and Liu, Baoli and Feng, Ji. Valley-selective circular dichroism of monolayer molybdenum disulphide. *Nature Communications* **2012**, *3*. <https://doi.org/10.1038/ncomms1882>.
18. Lagarde, D. and Bouet, L. and Marie, X. and Zhu, C. R. and Liu, B. L. and Amand, T. and Tan, P. H. and Urbaszek, B.. Carrier and Polarization Dynamics in Monolayer MoS<sub>2</sub>. *Phys. Rev. Lett.* **2014**, *112*, 047401. <https://doi.org/10.1103/PhysRevLett.112.047401>.
19. Plechinger, G. and Nagler, P. and C. Schüller, C. and Korn, T.. Time-resolved Kerr rotation spectroscopy of valley dynamics in single-layer MoS<sub>2</sub>. *arXiv:1404.7674* **2014**.
20. Zhu, C. R. and Zhang, K. and Glazov, M. and Urbaszek, B. and Amand, T. and Ji, Z. W. and Liu, B. L. and Marie, X.. Exciton valley dynamics probed by Kerr rotation in WSe<sub>2</sub> monolayers. *Phys. Rev. B* **2014**, *90*, 161302. <https://doi.org/10.1103/PhysRevB.90.161302>.
21. Dal Conte, S. and Bottegoni, F. and Pogna, E. A. A. and De Fazio, D. and Ambrogio, S. and Bargigia, I. and D'Andrea, C. and Lombardo, A. and Bruna, M. and Ciccacci, F. and Ferrari, A. C. and Cerullo, G. and Finazzi, M.. Ultrafast valley relaxation dynamics in monolayer MoS<sub>2</sub> probed by nonequilibrium optical techniques. *Phys. Rev. B* **2015**, *92*, 235425. <https://doi.org/10.1103/PhysRevB.92.235425>.
22. Plechinger, G. and Nagler, Ph. and Arora, A. and Schmidt, R. and Chernikov, A. and Lupton, J. and Bratschitsch, R. and Schüller, Ch. and Korn, T.. Valley dynamics of excitons in monolayer dichalcogenides. *Phys. Stat. Solidi – Rapid Research Letters* **2017**, *11*, 1700131. <https://doi.org/https://doi.org/10.1002/pssr.201700131>.
23. Elizabeth J McCormick and Michael J Newburger and Yunqiu Kelly Luo and Kathleen M McCreary and Simranjeet Singh and Iwan B Martin and Edward J Cichewicz and Berend T Jonker and Roland K Kawakami. Imaging spin dynamics in monolayer WS<sub>2</sub> by time-resolved Kerr rotation microscopy. *2D Materials* **2017**, *5*, 011010. <https://doi.org/10.1088/2053-1583/aa98ae>.
24. Van der Donck, M. and Zarenia, M. and Peeters, F.M.. Strong valley Zeeman effect of dark excitons in monolayer transition metal dichalcogenides in a tilted magnetic field. *Phys. Rev. B* **2018**, *97*, 081109. <https://doi.org/10.1103/PhysRevB.97.081109>.
25. T.Y.T. Hung and K.Y. Camsari and S. Zhang and P. Upadhyaya and Z. Chen. Direct observation of valley-coupled topological current in MoS<sub>2</sub>. *Science Advances* **2019**, *5*, eaau6478. <https://doi.org/10.1126/sciadv.aau6478>.
26. Lin, K.-Q. *et al.* . Narrow-band high-lying excitons with negative-mass electrons in monolayer WSe<sub>2</sub>. *Nature Communications* **2021**, *12*. <https://doi.org/10.1038/s41467-021-25499-2>.
27. Lin, Kai-Qiang and Ziegler, Jonas D. and Semina, Marina A. and Mamedov, V, Javid and Watanabe, Kenji and Taniguchi, Takashi and Bange, Sebastian and Chernikov, Alexey and Glazov, Mikhail M. and Lupton, John M.. High-lying valley-polarized trions in 2D semiconductors. *Nature Communications* **2022**, *13*. <https://doi.org/10.1038/s41467-022-33939-w>.
28. Szcześniak, Dominik and Kais, Sabre. Gap states and valley-spin filtering in transition metal dichalcogenide monolayers. *Phys. Rev. B* **2020**, *101*, 115423. <https://doi.org/10.1103/PhysRevB.101.115423>.
29. Jonas Kiemle and Philipp Zimmermann and Alexander W. Holleitner and Christoph Kastl. Light-field and spin-orbit-driven currents in van der Waals materials. *Nanophotonics* **2020**, *9*, 2693–2708. <https://doi.org/doi:10.1515/nanoph-2020-0226>.
30. Caruso, F. and Schebek, M. and Pan, Y. and Vona, C. and Draxl, C.. Chirality of Valley Excitons in Monolayer Transition-Metal Dichalcogenides. *Journ. Phys. Chem. Lett.* **2022**, *13*, 5894–5899. <https://doi.org/10.1021/acs.jpcclett.2c01034>.
31. K. F. Mak and K. L. McGill and J. Park and P. L. McEuen . The valley Hall effect in MoS<sub>2</sub> transistors. *Science* **2014**, *344*, 1489–1492. <https://doi.org/10.1126/science.1250140>.
32. Rostami, H. and Volckaert, K. and Lanata, N. and Mahatha, S.K. and Sanders, C.E. and Bianchi, M. and Lizzit, D. and Bignardi, L. and Lizzit, S. and Miwa, J.A. and Balatsky, A.V. and Hofmann, Ph. and Ulstrup, S. . Layer and orbital interference effects in photoemission from transition metal dichalcogenides. *Phys. Rev. B* **2019**, *100*, 235423. <https://doi.org/10.1103/PhysRevB.100.235423>.
33. Wang, Qinsheng and Ge, Shaofeng and Li, Xiao and Qiu, Jun and Ji, Yanxin and Feng, Ji and Sun, Dong. Valley Carrier Dynamics in Monolayer Molybdenum Disulfide from Helicity-Resolved Ultrafast Pump–Probe Spectroscopy. *ACS Nano* **2013**, *7*, 11087–11093, [<https://doi.org/10.1021/nn405419h>]. <https://doi.org/10.1021/nn405419h>.
34. Mai, Cong and Barrette, Andrew and Yu, Yifei and Semenov, Yuriy G. and Kim, Ki Wook and Cao, Linyou and Gundogdu, Kenan. Many-Body Effects in Valleytronics: Direct Measurement of Valley Lifetimes in Single-Layer MoS<sub>2</sub>. *Nano Letters* **2014**, *14*, 202–206, [<https://doi.org/10.1021/nl403742j>]. <https://doi.org/10.1021/nl403742j>.
35. Yang, Luyi and Sinitsyn, Nikolai A. and Chen, Weibing and Yuan, Jiangtan and Zhang, Jing and Lou, Jun and Crooker, Scott A.. Long-lived nanosecond spin relaxation and spin coherence of electrons in monolayer MoS<sub>2</sub> and WS<sub>2</sub>. *Nature Physics* **2015**, *11*, 830–U187. <https://doi.org/10.1038/NPHYS3419>.
36. Molina-Sánchez, Alejandro and Sangalli, Davide and Wirtz, Ludger and Marini, Andrea. Ab Initio Calculations of Ultrashort Carrier Dynamics in Two-Dimensional Materials: Valley Depolarization in Single-Layer WSe<sub>2</sub>. *Nano Letters* **2017**, *17*, 4549–4555. PMID: 28692278, <https://doi.org/10.1021/acs.nanolett.7b00175>.

- 
37. Julien Levallois and Michaël Tran and Alexey B. Kuzmenko. Decrypting the cyclotron effect in graphite using Kerr rotation spectroscopy. *Solid State Communications* **2012**, *152*, 1294–1300. Exploring Graphene, Recent Research Advances, <https://doi.org/https://doi.org/10.1016/j.ssc.2012.04.036>.
  38. Levallois, Julien and Nedoliuk, Ievgeniia O. and Crassee, Iris and Kuzmenko, Alexey B.. Magneto-optical Kramers-Kronig analysis. *Review of Scientific Instruments* **2015**, *86*, 033906. <https://doi.org/10.1063/1.4914846>.
  39. G Catarina and N M R Peres and J Fernández-Rossier. Magneto-optical Kerr effect in spin split two-dimensional massive Dirac materials. *2D Materials* **2020**, *7*, 025011. <https://doi.org/10.1088/2053-1583/ab6781>.
  40. Kimel, A.V. and Kirilyuk, A. and Usachev, P.A. and Pisarev, R.V. and Balbashov, A.M. and Rasing, T.. Ultrafast non-thermal control of magnetization by instantaneous photomagnetic pulses. *Nature* **2005**, *435*, 655–657. <https://doi.org/10.1038/nature03564>.
  41. Yan, Tengfei and Yang, Siyuan and Li, Dian and Cui, Xiaodong. Long valley relaxation time of free carriers in monolayer WSe<sub>2</sub>. *Phys. Rev. B* **2017**, *95*, 241406. <https://doi.org/10.1103/PhysRevB.95.241406>.
  42. Michele Perlangeli and Simone Peli and Davide Soranzio and Denny Puntel and Fulvio Parmigiani and Federico Cilento. Polarization-resolved broadband time-resolved optical spectroscopy for complex materials: application to the case of MoTe<sub>2</sub> polytypes. *Opt. Express* **2020**, *28*, 8819–8829. <https://doi.org/10.1364/OE.385419>.
  43. Kormányos, Andor and Zólyomi, Viktor and Drummond, Neil D. and Rakyta, Péter and Burkard, Guido and Fal'ko, Vladimir I.. Monolayer MoS<sub>2</sub>: Trigonal warping, the  $\Gamma$  valley, and spin-orbit coupling effects. *Phys. Rev. B* **2013**, *88*, 045416. <https://doi.org/10.1103/PhysRevB.88.045416>.
  44. Andor Kormányos and Guido Burkard and Martin Gmitra and Jaroslav Fabian and Viktor Zólyomi and Neil D Drummond and Vladimir Fal'ko.  $\mathbf{k} \cdot \mathbf{p}$  theory for two-dimensional transition metal dichalcogenide semiconductors. *2D Materials* **2015**, *2*, 022001. <https://doi.org/10.1088/2053-1583/2/2/022001>.
  45. Rostami, Habib and Roldán, Rafael and Cappelluti, Emmanuele and Asgari, Reza and Guinea, Francisco. Theory of strain in single-layer transition metal dichalcogenides. *Phys. Rev. B* **2015**, *92*, 195402. <https://doi.org/10.1103/PhysRevB.92.195402>.
  46. Rostami, Habib and Moghaddam, Ali G. and Asgari, Reza. Effective lattice Hamiltonian for monolayer MoS<sub>2</sub>: Tailoring electronic structure with perpendicular electric and magnetic fields. *Phys. Rev. B* **2013**, *88*, 085440. <https://doi.org/10.1103/PhysRevB.88.085440>.
  47. Cappelluti, E. and Roldán, R. and Silva-Guillén, J. A. and Ordejón, P. and Guinea, F.. Tight-binding model and direct-gap/indirect-gap transition in single-layer and multilayer MoS<sub>2</sub>. *Phys. Rev. B* **2013**, *88*, 075409. <https://doi.org/10.1103/PhysRevB.88.075409>.
  48. Zahid, Ferdows and Liu, Lei and Zhu, Yu and Wang, Jian and Guo, Hong. A generic tight-binding model for monolayer, bilayer and bulk MoS<sub>2</sub>. *AIP Advances* **2013**, *3*, 052111. <https://doi.org/10.1063/1.4804936>.
  49. Wu, F. and Qu, F. and MacDonald, A.H.. Exciton band structure of monolayer MoS<sub>2</sub>. *Phys. Rev. B* **2015**, *91*, 075310. <https://doi.org/10.1103/PhysRevB.91.075310>.
  50. Fang, Shiang and Kuate Defo, Rodrick and Shirodkar, Sharmila N. and Lieu, Simon and Tritsarlis, Georgios A. and Kaxiras, Efthimios. Ab initio tight-binding Hamiltonian for transition metal dichalcogenides. *Phys. Rev. B* **2015**, *92*, 205108. <https://doi.org/10.1103/PhysRevB.92.205108>.
  51. E. Ridolfi and D. Le and T.S. Rahman and E.R. Mucciolo and C.H. Lewenkopf. A tight-binding model for MoS<sub>2</sub> monolayers. *Journal of Physics: Condensed Matter* **2015**, *27*, 365501. <https://doi.org/10.1088/0953-8984/27/36/365501>.
  52. Dias, A.C. and Qu, F. and Azevedo, D.L. and Fu, J.. Band structure of monolayer transition-metal dichalcogenides and topological properties of their nanoribbons: Next-nearest-neighbor hopping. *Phys. Rev. B* **2018**, *98*, 075202. <https://doi.org/10.1103/PhysRevB.98.075202>.
  53. Bert Jorissen and Lucian Covaci and Bart Partoens. Comparative analysis of tight-binding models for transition metal dichalcogenides. *SciPost Phys. Core* **2024**, *7*, 004. <https://doi.org/10.21468/SciPostPhysCore.7.1.004>.
  54. Liu, Gui-Bin and Shan, Wen-Yu and Yao, Yugui and Yao, Wang and Xiao, Di. Three-band tight-binding model for monolayers of group-VIB transition metal dichalcogenides. *Phys. Rev. B* **2013**, *88*, 085433. <https://doi.org/10.1103/PhysRevB.88.085433>.
  55. R. Roldán and M.P. López-Sancho and F. Guinea and E. Cappelluti and J.A. Silva-Guillén and P. Ordejón. Momentum dependence of spin-orbit interaction effects in single-layer and multi-layer transition metal dichalcogenides. *2D Materials* **2014**, *1*, 034003. <https://doi.org/10.1088/2053-1583/1/3/034003>.
  56. Carvalho, A.; Ribeiro, R.M.; Castro Neto, A.H. Band nesting and the optical response of two-dimensional semiconducting transition metal dichalcogenides. *Phys. Rev. B* **2013**, *88*, 115205. <https://doi.org/10.1103/PhysRevB.88.115205>.
  57. Gibertini, Marco and Pellegrino, Francesco M. D. and Marzari, Nicola and Polini, Marco. Spin-resolved optical conductivity of two-dimensional group-VIB transition-metal dichalcogenides. *Phys. Rev. B* **2014**, *90*, 245411. <https://doi.org/10.1103/PhysRevB.90.245411>.
  58. Kozawa, Daichi and Kumar, Rajeev and Carvalho, Alexandra and Amara, Kiran Kumar and Zhao, Weijie and Wang, Shunfeng and Toh, Minglin and Ribeiro, Ricardo M. and Castro Neto, A. H. and Matsuda, Kazunari and Eda, Goki. Photocarrier relaxation pathway in two-dimensional semiconducting transition metal dichalcogenides. *Nature Communications* **2014**, *5*. <https://doi.org/10.1038/ncomms5543>.
  59. Bertoni, R.; Nicholson, C.W.; Waldecker, L.; Hübener, H.; Monney, C.; De Giovannini, U.; Puppini, M.; Hoesch, M.; Springate, E.; Chapman, R.T.; et al. Generation and Evolution of Spin-, Valley-, and Layer-Polarized Excited Carriers in Inversion-Symmetric WSe<sub>2</sub>. *Phys. Rev. Lett.* **2016**, *117*, 277201. <https://doi.org/10.1103/PhysRevLett.117.277201>.

- 
60. Schmidt, Robert and Berghäuser, Gunnar and Schneider, Robert and Selig, Malte and Tonndorf, Philipp and Malić, Ermin and Knorr, Andreas and Michaelis de Vasconcellos, Steffen and Bratschitsch, Rudolf. Ultrafast Coulomb-Induced Intervalley Coupling in Atomically Thin WS<sub>2</sub>. *Nano Letters* **2016**, *16*, 2945–2950. PMID: 27086935, <https://doi.org/10.1021/acs.nanolett.5b04733>.
  61. Yan, Tengfei and Yang, Siyuan and Li, Dian and Cui, Xiaodong. Long valley relaxation time of free carriers in monolayer WSe<sub>2</sub>. *Phys. Rev. B*.
  62. Yu, T. and Wu, M. W.. Valley depolarization due to intervalley and intravalley electron-hole exchange interactions in monolayer MoS<sub>2</sub>. *Phys. Rev. B* **2014**, *89*, 205303. <https://doi.org/10.1103/PhysRevB.89.205303>.
  63. Bertoni, R. and Nicholson, C. W. and Waldecker, L. and Hübener, H. and Monney, C. and De Giovannini, U. and Puppini, M. and Hoesch, M. and Springate, E. and Chapman, R. T. and Cacho, C. and Wolf, M. and Rubio, A. and Ernstorfer, R.. Generation and Evolution of Spin-, Valley-, and Layer-Polarized Excited Carriers in Inversion-Symmetric WSe<sub>2</sub>. *Phys. Rev. Lett.* **2016**, *117*, 277201. <https://doi.org/10.1103/PhysRevLett.117.277201>.

**Disclaimer/Publisher's Note:** The statements, opinions and data contained in all publications are solely those of the individual author(s) and contributor(s) and not of MDPI and/or the editor(s). MDPI and/or the editor(s) disclaim responsibility for any injury to people or property resulting from any ideas, methods, instructions or products referred to in the content.